

Super-resolution imaging of non-fluorescent reactions via competition

Xianwen Mao¹, Chunming Liu¹, Mahdi Hesari¹, Ningmu Zou^{1,2} and Peng Chen^{1*}

Super-resolved fluorescence microscopy techniques have enabled substantial advances in the chemical and biological sciences. However, they can only interrogate entities that fluoresce, and most chemical or biological processes do not involve fluorescent species. Here we report a competition-enabled imaging technique with super-resolution (COMPEITS) that enables quantitative super-resolution imaging of non-fluorescent processes. It is based on the incorporation of competition into a single-molecule fluorescence-detection scheme. We demonstrate COMPEITS by investigating a photoelectrocatalytic reaction; we map, with nanometre precision, a non-fluorescent surface reaction that is important for water decontamination on single photocatalyst particles. The subparticle-level quantitative information of reactant adsorption affinities unambiguously decouples size- and shape-scaling laws on specific particle facets and uncovers a surprising biphasic shape dependence, leading to catalyst design principles for optimal reactant adsorption efficacy. With its ability to provide spatially resolved information on the behaviours of unlabelled, non-fluorescent entities under operando conditions, COMPEITS could interrogate a variety of surface processes in fields ranging from heterogeneous catalysis and materials engineering to nanotechnology and energy sciences.

The development of high-resolution imaging techniques, such as electron^{1,2} and X-ray microscopy-based³ and scanning probe-based approaches^{4–6}, has brought tremendous advances to the physical and life sciences. Among them, optical microscopy-based imaging methods^{7–13} are arguably the most widely used; they allow for non-invasive, real-time in situ observation of structures and dynamics under realistic conditions (for example, in liquid environments), which is challenging to achieve using non-optical methods that usually operate either in vacuo or under ex situ conditions. However, conventional optical microscopy has a diffraction-limited resolution of about 200–300 nm. This diffraction limit was breached recently by super-resolved fluorescence microscopy (which reached a resolution of ~10 nm), including techniques that are based on point-spread-function engineering, such as stimulated emission depletion microscopy¹¹, or on single-molecule localization, such as photoactivated localization microscopy¹² and stochastic optical reconstruction microscopy¹³.

These super-resolution techniques have revolutionized many research fields, particularly biology^{7,12–19}, not just because of their resolution, but also their ease in experimental implementation. More recently, single-molecule-localization-based methods have been applied to image fluorogenic surface reactions with nanometre resolution, yielding site-specific activity and dynamics within single catalyst particles^{20–26}. Nonetheless, all of these super-resolution imaging techniques can only study entities or processes that fluoresce or are fluorescently labelled, whereas most chemical or biological processes do not involve fluorescent species. A recently introduced MINFLUX approach has substantially reduced the number of fluorescence photons that are needed to achieve nanometre spatial resolution, but this approach still targets fluorescent processes¹⁸. Here we report a competition-enabled imaging technique with super-resolution (COMPEITS) that, by exploiting a competition strategy, could interrogate non-fluorescent processes at nanometre resolution and is easy to implement experimentally.

Results

The design and generality of COMPEITS. Figure 1a illustrates the concept of COMPEITS, using a surface-catalysed reaction as an example (experiment and data processing details are in the Methods, Supplementary Sections 1.1–1.4, Supplementary Tables 1–4 and Supplementary Figs. 1–6). A solid particle catalyses an auxiliary fluorogenic reaction, whose fluorescent product molecules can be imaged and localized individually at nanometre resolution. The reaction of interest can be catalysed by the same particle, but neither the reactants nor the products are fluorescent. This non-fluorescent reaction competes for the same surface sites on the catalyst particle where the fluorogenic reaction occurs, which leads to suppression of the fluorogenic reaction rate. The extent of suppression can be imaged at the same nanometre resolution as the fluorogenic reaction, yielding super-resolution spatial information on the non-fluorescent reaction.

COMPEITS is highly generalizable and broadly applicable to many critical processes in chemistry, biology and materials science (Supplementary Section 2.1). It can spatially map any non-fluorescent process that suppresses, enhances the intensity or alters the emission wavelength of an auxiliary fluorescent process. For example, the target non-fluorescent process of COMPEITS could be competitions or inhibitions of surface- or enzyme-catalysed reactions such as fluorescence quenchers and redox mediators^{27–30}. The auxiliary systems could be fluorogenic reactions (Fig. 1a), blinking molecules/particles or any fluorescent processes that can be imaged by super-resolution microscopy.

Here, we apply COMPEITS to study photoelectrocatalysis, a process of fundamental and technological importance for a wide range of applications such as environmental remediation and energy conversion³¹. We chose bismuth vanadate (BiVO₄) as the photocatalyst because of its visible absorption when collecting solar energy³¹ and morphological and compositional tunability for photocatalytic performance^{32,33}. We prepared BiVO₄ particles with a tunable truncated bipyramid morphology³³ that is quantifiable by a size

¹Department of Chemistry and Chemical Biology, Cornell University, Ithaca, NY, USA. ²Present address: AMD Inc., Austin, TX, USA.

*e-mail: pc252@cornell.edu

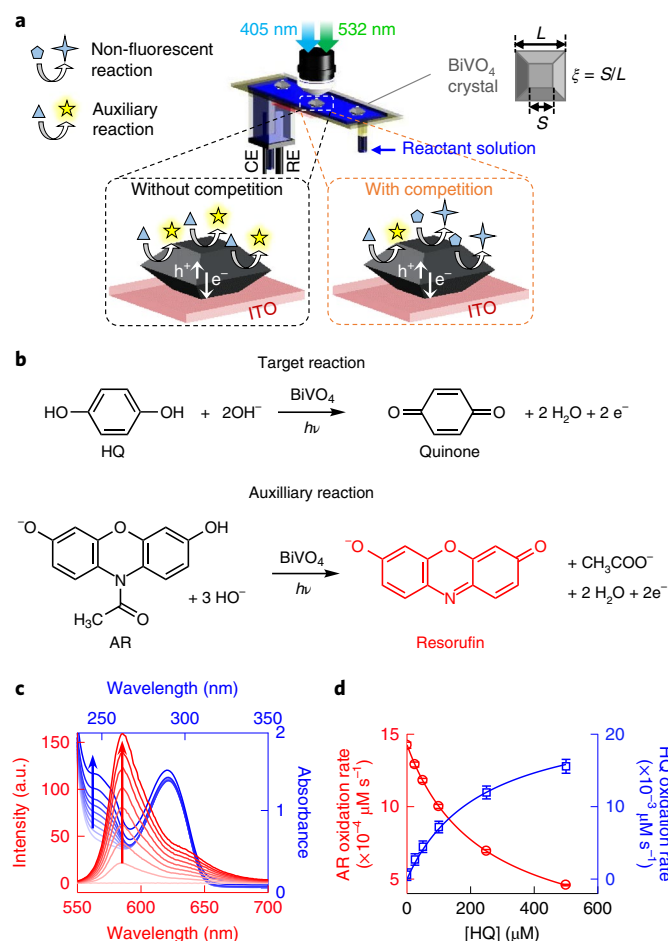


Figure 1 | A demonstration of COMPEITS using a surface reaction.

a, The COMPEITS set-up, which uses wide-field fluorescence microscopy in a photoelectrocatalytic microfluidic cell via two-laser epifluorescence illumination (Supplementary Section 1.3). Here, a catalyst particle can catalyse both a non-fluorescent reaction and an auxiliary fluorogenic reaction; the fluorescent signals collected depend on the degree of competition between the two reactions. CE, counter electrode; RE, reference electrode. **b**, The target and auxiliary reactions. **c**, Time-dependent (0–40 min, indicated by the arrows) absorption of quinone (blue) and fluorescence of resorufin (red) during simultaneous photoelectrocatalysis of the two competing reactions on bulk BiVO₄ films, showing that the products of the two reactions were generated under this catalytic condition. The initial [HQ] and [AR] are 500 μM and 40 μM , respectively. **d**, The HQ or AR oxidation rate (blue or red symbols) versus [HQ], demonstrating the competition between the two reactions. The lines are fits with equation (1) and Supplementary Equation 1. Error bars represent the standard deviation.

parameter L and a shape parameter ξ ($=S/L$, see the inset of Fig. 1a and Supplementary Fig. 1): L ranges from ~ 1 to 10 μm , whereas ξ varies from ~ 0.3 (square-bipyramid-like) to ~ 1 (square-plate-like) (Supplementary Table 5).

Our target non-fluorescent reaction is the photoelectrocatalytic oxidation of hydroquinone (HQ) (Fig. 1b), a primary phenolic micro-pollutant in aquatic ecosystems^{34,35} and a prevalent redox mediator on (photo)electrodes and in biology³⁶. The auxiliary fluorogenic reaction that competes with HQ oxidation is the oxidation of amplex red (AR) (Fig. 1b), which generates resorufin, a fluorescent molecule²².

First, we demonstrated the competition between AR and HQ oxidations photoelectrocatalytically by using a bulk BiVO₄

electrode (405 nm illumination with an applied potential of 0.2 V; all potentials refer to Ag/AgCl). We monitored the fluorescence of resorufin and the absorption of quinone, the two respective products (Fig. 1b). Both products are observed, confirming that HQ and AR are oxidizable by the photogenerated holes in BiVO₄, as is expected from their oxidation potentials (Supplementary Fig. 11). There is no discernible HQ or AR oxidation without 405 nm illumination (Supplementary Fig. 12). More importantly, at a fixed AR concentration ([AR]), the rate of quinone formation increases with increasing [HQ], while the rate of resorufin formation decreases concurrently (Fig. 1d), as is expected for competing reactions. By varying [AR], we further show that the AR–HQ system follows a competitive inhibition behaviour, whereby the two reactants compete for the same catalyst surface sites (Supplementary Section 2.5). The AR oxidation reaction rate follows saturation kinetics with competitive inhibition by HQ (Supplementary Section 1.2)³⁷:

$$v_{\text{AR}} = \frac{k_{\text{AR}}K_{\text{AR}}[\text{AR}]}{1 + K_{\text{AR}}[\text{AR}] + K_{\text{HQ}}[\text{HQ}]} \quad (1)$$

where k_{AR} is the (specific) rate constant and v_{AR} the (specific) rate of the AR oxidation reaction; K_{AR} and K_{HQ} are the adsorption equilibrium constants for AR and HQ on the catalyst surface, respectively. Supplementary Equation 1 gives a similar equation for v_{HQ} , the (specific) rate of HQ oxidation. Both equations describe the bulk kinetics satisfactorily (Fig. 1d). Moreover, v_{AR}^{-1} from equation (1) scales linearly with [HQ], with the scaling constant $K_{\text{HQ}}/(k_{\text{AR}}K_{\text{AR}}[\text{AR}])$, which is directly proportional to K_{HQ} .

COMPEITS imaging of HQ oxidation on single particles. To perform COMPEITS imaging on the photoelectrocatalytic oxidation of HQ, we dispersed BiVO₄ particles on a transparent indium-doped tin oxide (ITO) electrode in a microfluidic photoelectrochemical cell (Fig. 1a). Continuous wide-field 405 nm laser illumination generates charge carriers in BiVO₄. At a positive potential (for example, 0.2 V), AR and HQ are oxidized on the surfaces of BiVO₄ particles; the fluorescence of resorufin from AR oxidation is induced by a 532 nm laser and imaged at super-resolution.

Figure 2a shows a quantitative super-resolution image of the auxiliary fluorogenic AR oxidation reaction on a single BiVO₄ particle relative to its scanning electron microscopy (SEM) image (Fig. 2e), where each fluorescent product is localized to ~ 40 nm precision (limited by the signal-to-noise ratio at a time resolution of 15 ms; Supplementary Section 1.3, 1.4). Following the introduction of the non-fluorescent HQ oxidation reaction, the number of detected AR oxidation products (n_p) decreases substantially with increasing [HQ] across the particle surface, reporting the competition (Fig. 2bi–biv). The direct difference (that is, Δn_p) images (Fig. 2ci–civ) show the expected trend: Δn_p becomes larger with higher [HQ]. It is worth noting that the direct difference does not scale linearly with K_{HQ} (as can be deduced from equation (1)), and thus its value does not directly manifest the adsorption strength of the competitor HQ.

Alternatively, the inverse difference image (Fig. 2di–div)—which we term the COMPEITS image—is more informative, and is obtained from calculating the difference in n_p^{-1} following the introduction of competition. From equation (1): $v_{\text{AR}}^{-1} \propto \frac{K_{\text{HQ}}}{k_{\text{AR}}K_{\text{AR}}[\text{AR}]}$ [HQ], and, therefore, at any fixed [AR] and between two different [HQ], the difference in v_{AR}^{-1} , that is, $\Delta(v_{\text{AR}}^{-1})$, is directly proportional to K_{HQ} . Moreover, n_p over any time period is linearly proportional to v_{AR} ; therefore, $\Delta(n_p^{-1})$ is also proportional to K_{HQ} and directly reflects the HQ binding affinity (see Supplementary equations 2–4).

The COMPEITS images in Fig. 2di–div immediately show that on this BiVO₄ particle, HQ adsorbs more strongly on the basal {010} facet than the lateral {110} facet. Moreover, within the lateral facets,

HQ adsorption is weaker at the corners where two lateral facets intersect at an edge. These subparticle- and subfacet-level differences represent a quantitative super-resolution mapping of non-fluorescent chemical processes (that is, HQ adsorption for subsequent oxidation here), enabled by COMPEITS (see Supplementary Fig. 14 for more COMPEITS images). Such quantitative adsorption information is crucial for surface reactions, especially for reactions of micropollutants such as HQ, whose low concentrations in the environment³⁵ dictate that their surface reaction rates scale linearly with their adsorption affinities (Supplementary Section 2.1).

COMPEITS images allow each particle to be dissected into basal and lateral facets and ν_{AR} titrated against the competing reactant concentration ([HQ]). At a fixed [AR], the ν_{AR}^{-1} of each facet increases linearly with increasing [HQ] (Fig. 2h,i), with the slope directly reflecting the magnitude of K_{HQ} , as predicted by equation (1). Fitting the data yields facet-specific K_{HQ} for each particle, which are inaccessible from ensemble-averaged measurements (K_{AR} in equation (1) was obtained from an earlier [AR] titration; Supplementary Section 1.3 and Supplementary Fig. 3; and ν_{AR} was also corrected to take into account the different illuminations at the top and bottom facets of a BiVO_4 particle, although such corrections do not affect K_{AR} and K_{HQ} ; Supplementary Section 1.4.3.2, 1.4.3.3).

COMPEITS can provide quantitative information of the target non-fluorescent reaction as long as the binding affinities of both the pro-fluorescent and non-fluorescent reactants can be accurately determined by titration (that is, $1/K_{\text{AR}}$ and $1/K_{\text{HQ}}$ are in experimentally titratable concentration regimes). As long as the two reactants would bind to the same or overlapping surface sites (which could be dependent on the relative molecule size), competition between the surface adsorption processes of the two molecules will occur (for a detailed discussion on the applicability of COMPEITS, see Supplementary Section 2.1).

Decoupling the size and shape effects of facet-specific reactant adsorption. After pooling the results from many BiVO_4 particles, the K_{HQ} for the basal {010} and lateral {110} facets ($K_{\text{HQ}}^{\{010\}}$ and $K_{\text{HQ}}^{\{110\}}$, respectively) show dispersion, but, on average, $K_{\text{HQ}}^{\{010\}}$ is more than two times larger than $K_{\text{HQ}}^{\{110\}}$, which indicates stronger HQ adsorption on the basal facet (see the two histograms in Fig. 3a,b), consistent with the COMPEITS images in Fig. 2d. Interestingly, $K_{\text{HQ}}^{\{010\}}$ and $K_{\text{HQ}}^{\{110\}}$ both show strong dependences on L . At any fixed ξ , both $K_{\text{HQ}}^{\{010\}}$ and $K_{\text{HQ}}^{\{110\}}$ decrease asymptotically with increasing L , probably due to the size dependence of particle surface energy (Fig. 3a,b, bottom left). These trends are clearer when $K_{\text{HQ}}^{\{010\}}$ and $K_{\text{HQ}}^{\{110\}}$ are projected onto the L axis (Fig. 3a,b, top left): $K_{\text{HQ}}^{\{010\}}$ and $K_{\text{HQ}}^{\{110\}}$ exhibit strong negative correlations with L , with the Pearson cross-correlation coefficients (ρ) being about -0.8 and -0.6 , respectively.

The adsorption equilibrium constants for the two facets, $K_{\text{HQ}}^{\{010\}}$ and $K_{\text{HQ}}^{\{110\}}$, also show clear dependences on ξ (Fig. 3a,b, bottom right). Both decrease asymptotically as the particle shape transitions from bipyramid-like to plate-like (that is, with increasing ξ). We hypothesized that this shape dependence may stem from their surrounding edges, which could differ from the facets in binding molecules and whose contributions around each facet vary with the particle shape. We therefore examined two edge regions (type I and type II) between the basal and lateral facets, and between the lateral facets, respectively (Fig. 2g). Type-I edges surround basal and lateral facets, and thus should affect the properties of both, whereas type-II edges should only contribute to those of the lateral facet. Hydroquinone titrations in COMPEITS images for these two edge regions gave their respective K_{HQ} (Fig. 2j,k). For most BiVO_4 particles, the ratios of K_{HQ} between the type-I edge and the facets are clearly different from unity (Fig. 3c,d), which indicates pronounced edge effects. The two types of edges also differ from each other, with the type-I edge on average having a larger K_{HQ} (Fig. 3e).

We further modelled the size and shape dependences of facet-specific K_{HQ} (see Supplementary Section 2.8 for the derivation):

$$K_{\text{HQ}} = \beta_i \exp\left(\frac{\beta_2}{L}\right) \exp(-\beta_3 \xi) \quad (2)$$

where β_i ($i=1, 2$ or 3) are scaling parameters (Supplementary Table 6). Equation (2) fits the data satisfactorily, giving the values of each β_i , and allowing us to predict K_{HQ} for individual facets over the experimental accessible ranges of the L and ξ values (Fig. 3a,b, lower left, shaded surfaces).

Particle morphology design principles for optimal reactant chemisorption. The fitted β_i parameters for the basal and lateral facets immediately allowed prediction of the overall HQ adsorption equilibrium constant ($K_{\text{HQ}}^{\text{whole}}$) for a whole BiVO_4 particle of any physically accessible size and shape ($L \approx 1\text{--}10 \mu\text{m}$; $\xi \approx 0.3\text{--}0.8$; Supplementary Table 5); $K_{\text{HQ}}^{\text{whole}}$ is the surface-area-weighted average of its composing facets, because K_{HQ} is a per-surface-site-based property (Supplementary Fig. 17 and Supplementary Section 2.10). Note the edge regions are part of the facets as defined in Fig. 2f). Compared with $K_{\text{HQ}}^{\{010\}}$ and $K_{\text{HQ}}^{\{110\}}$, $K_{\text{HQ}}^{\text{whole}}$ is a parameter that directly assesses how effectively a whole BiVO_4 catalyst particle adsorbs the target pollutant HQ at the per-surface site level.

More importantly, we could define and predict

$$\omega_{\text{HQ}} \equiv K_{\text{HQ}}^{\text{whole}} \frac{A}{V} \quad (3)$$

which normalizes $K_{\text{HQ}}^{\text{whole}}$ by the particle volume (V) and multiplies it by the particle surface area (A). As such, ω_{HQ} quantifies the particle's overall capability of adsorbing the aqueous micropollutant HQ on its entire surface at the per-unit-mass level. The materials economy in assessing the adsorption efficacy of the catalyst particle is therefore taken into account by ω_{HQ} . The values of ω_{HQ} predicted from the fitted β_i parameters agree well with the experimental values obtained from whole particle COMPEITS titrations (Fig. 4a). The global maximum of ω_{HQ} corresponds with the smallest possible plate-like particles (for example, $\xi = 0.8$, $L = 1 \mu\text{m}$). At any fixed ξ , ω_{HQ} always decays with increasing L . And, plate-like particles (particles with larger ξ) exhibit steeper decays with increasing L than bipyramid-like particles (particles with smaller ξ) (Fig. 4a, top). This is understandable because, compared with bipyramid-like particles, plate-like particles comprise a larger fraction of the basal {010} facet, whose HQ adsorption ability decays more quickly with increasing L than that of the lateral {110} facet (that is, the size-scaling parameter β_2 for $K_{\text{HQ}}^{\{010\}}$ is larger than for $K_{\text{HQ}}^{\{110\}}$).

Depending on L , the unit-mass-level whole-particle adsorption equilibrium constant ω_{HQ} shows three distinct dependences on ξ (Fig. 4a, right). For smaller particles ($L < \sim 2.3 \mu\text{m}$), the optimal shape for larger ω_{HQ} is plate-like (larger ξ), whereas for larger particles ($L > \sim 9 \mu\text{m}$) a bipyramid-like shape (smaller ξ) is better. Interestingly, for particles of intermediate sizes ($\sim 2.3 \mu\text{m} < L < \sim 9 \mu\text{m}$), ω_{HQ} versus ξ shows a biphasic behaviour with a minimum; the optimal shape to maximize ω_{HQ} is either plate-like or bipyramid-like, but not a truncated bipyramid. These distinct behaviours accentuate the complexity of catalyst particle properties and represent a new identification of size- and shape-optimized catalyst particles, which is made possible by COMPEITS for reactant adsorption in a micropollutant degradation reaction here.

To understand the three distinct shape dependences of ω_{HQ} , we compared $K_{\text{HQ}}^{\{010\}}$ with $K_{\text{HQ}}^{\{110\}}$ in the physically accessible (L , ξ) space (Fig. 4b, top). Although on average $K_{\text{HQ}}^{\{010\}} > K_{\text{HQ}}^{\{110\}}$, this relation is not always true, and is valid only for smaller particles (smaller L). When L increases, a cross-over line appears because of the steeper

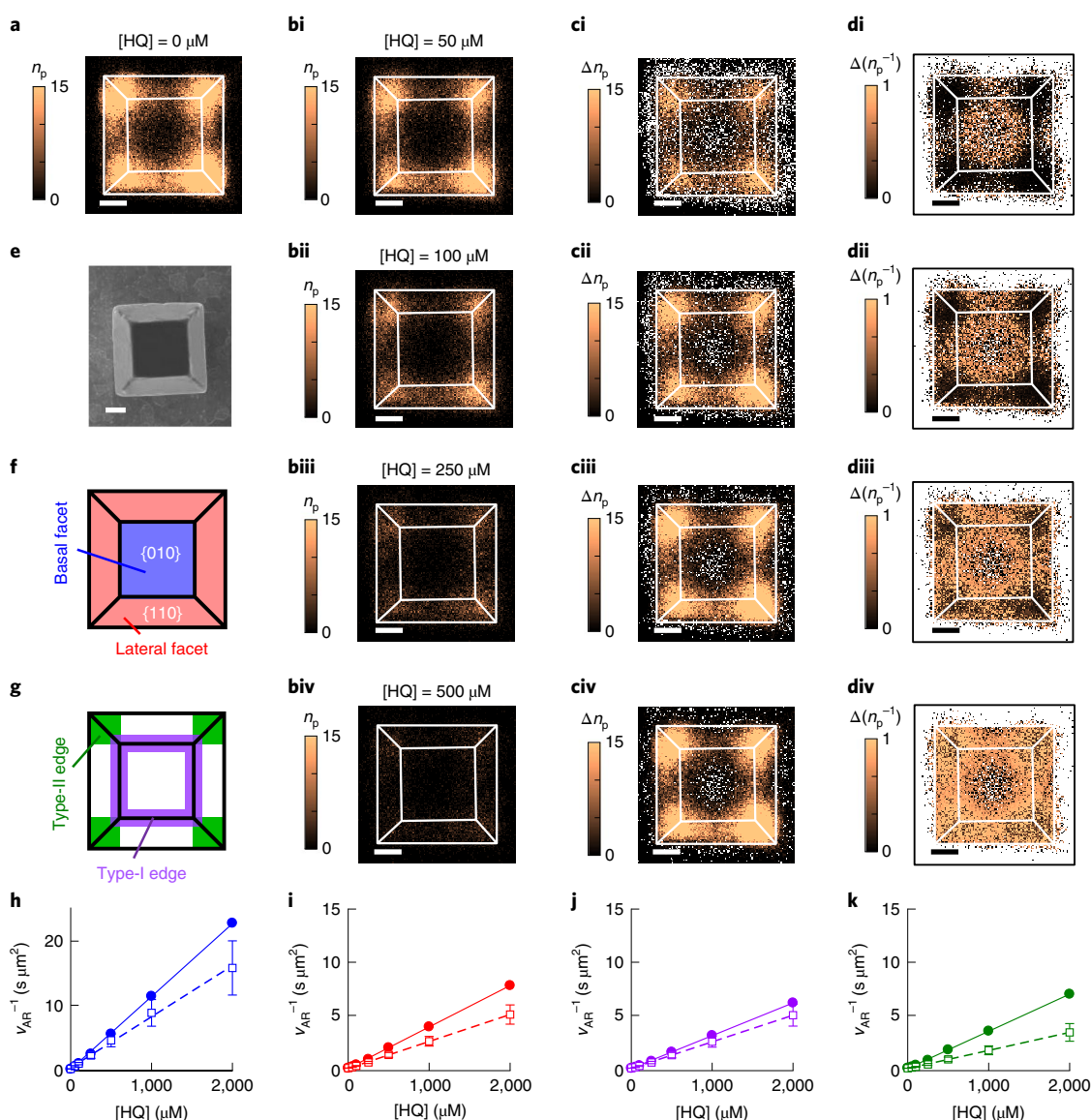


Figure 2 | COMPEITS imaging of the photoelectrooxidation of HQ on single BiVO₄ particles. **a**, An image plot (that is, a two-dimensional (2D) histogram) of n_p over 22.5 min without HQ. **bi–biv**, Image plots of n_p over 22.5 min with 50 μM (**bi**), 100 μM (**bii**), 250 μM (**biii**) and 500 μM (**biv**) HQ. In **a** and **b**, [AR] = 50 nM; the bin size is 33 \times 33 nm²; and white lines are structural contours determined from the SEM image in **e**. **ci–civ**, Images derived from Δn_p between **a** and **bi–biv**. White/null pixels represent the occasional negative values. **di–div**, COMPEITS images derived from $\Delta(n_p^{-1})$ between **a** and **bi–biv**. White/null pixels represent the occasional negative values or infinities due to 1/0 (that is, the bin has zero detected product molecules). **e**, An SEM image of the BiVO₄ particle in **a–d**. **f**, An illustration of the basal {010} and lateral {110} facets. **g**, Definition of the type-I and type-II edge regions. For the type-I region, the width on either side of the black edge is chosen to be 50 nm, which is slightly larger than the localization error (~40 nm). **h–k**, The ν_{AR}^{-1} of the auxiliary reaction versus [HQ] at [AR] = 50 nM for the basal {010} (**h**) and lateral {110} facets (**i**), and the type-I (**j**) and type-II edges (**k**). Solid circles represent the particle in **a–e**; open squares are the averages of 42 particles; lines are fits with equation (1). The plots of ν_{AR}^{-1} versus [HQ] are shown in Supplementary Fig. 15. All scale bars are 500 nm. All error bars are the s.e.m.

decays of $K_{\text{HQ}}^{(010)}$ with increasing L (yellow dashed line, Fig. 4b, bottom), after which the relation reverses. This cross-over behaviour underlies the three different shape dependences of ω_{HQ} (Fig. 4b, bottom). When L is very small, $K_{\text{HQ}}^{(010)} > K_{\text{HQ}}^{(110)}$, and a plate-like shape that has more basal {010} facets thus has a larger ω_{HQ} . Conversely, when L is very large, $K_{\text{HQ}}^{(010)} < K_{\text{HQ}}^{(110)}$, and a bipyramid-like shape that has more lateral {110} facets thus has a larger ω_{HQ} . At the intermediate L values, a transition regime exists, where the optimal shape for large ω_{HQ} is either plate- or bipyramid-like. The boundaries of the transition regime for ω_{HQ} (Fig. 4a, lower left) are shifted from the cross-over line of K_{HQ} (Fig. 4b, bottom), because ω_{HQ} which

is a unit-mass-based quantity, contains the surface-to-volume ratio (A/V) that is also size and shape dependent.

Discussion

We have developed COMPEITS to image and quantify at super-optical resolution the chemisorption of the non-fluorescent reactant molecule HQ, a micropollutant in aquatic ecosystems, on single BiVO₄ photocatalyst particles under photoelectrocatalysis conditions. This quantitative imaging enables unambiguous deconvolution of the effects of size and shape on the properties of specific facets of single catalyst particles. We find that, surprisingly, the HQ binding affinity on each facet exhibits particle shape dependence,

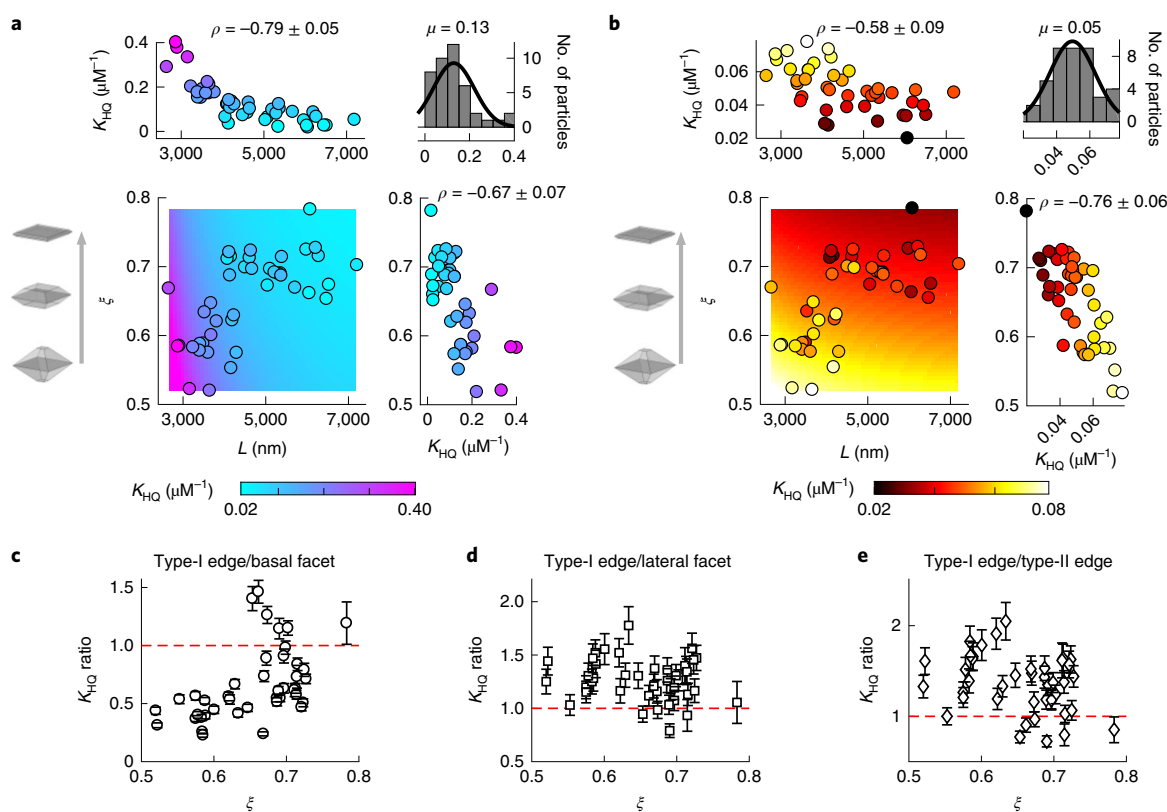


Figure 3 | Subparticle, facet-specific size and shape dependences of HQ binding affinity. **a, b**, Bottom left, the 2D dependences of K_{HQ} on L and ξ for the basal {010} (**a**) and lateral {110} facets (**b**) are shown, demonstrating the decoupling of the dependency of K_{HQ} on L and ξ . Each circle represents one particle of a total of 42. The shaded surfaces are fits with equation (2). For the basal {010} facet, $\beta_1 = 0.11 \pm 0.05 \mu\text{M}^{-1}$, $\beta_2 = 8360 \pm 700 \text{ nm}$ and $\beta_3 = 3.06 \pm 0.66$. For the lateral {110} facet, $\beta_1 = 0.23 \pm 0.11 \mu\text{M}^{-1}$, $\beta_2 = 830 \pm 620 \text{ nm}$ and $\beta_3 = 2.65 \pm 0.56$. Top left and bottom right, the corresponding one-dimensional projections of K_{HQ} data onto the L and ξ axes are shown, respectively, demonstrating that K_{HQ} is negatively correlated with L and ξ . Top right, the distribution of K_{HQ} of individual BiVO_4 particles is shown, demonstrating that, on average, K_{HQ} is larger for the basal {010} facet than for the lateral {110} facet; μ is the particle-averaged K_{HQ} . **c–e**, The selected K_{HQ} ratios between the type-I edge and the basal {010} facet (**c**), the type-I edge and the lateral {110} facet (**d**), and the type-I and type-II edges (**e**) versus ξ . Other types of ratio are shown in Supplementary Fig. 16. The error bars represent the s.d.

and we identify that this shape dependence originates from pronounced edge effects, whereby different particle shapes give rise to varying contributions of edges to each facet. Moreover, the overall HQ adsorption efficacy of a whole particle exhibits three distinct types of shape dependences. In particular, within an intermediate size regime, this overall adsorption efficacy shows striking biphasic dependences on the particle shape. These insights offer a basis for the rational design of photocatalysts for optimal water decontamination performance, indicating the need for combined size and shape engineering of catalyst particles.

COMPEITS could, in principle, image a broad range of non-fluorescent processes at nanometre resolution, in situ and under operando conditions. The application of COMPEITS here yielded particle-size/shape-decoupled information for an important pollutant degradation reaction on specific particle facets. However, COMPEITS has its limitations. It still requires an auxiliary fluorescent process as a reporter. Its capability to monitor dynamic processes is limited, as both the concentration titration of the competing reactant and the accumulation of many single-molecule localizations require a fairly long imaging duration (for example, tens of minutes). For the HQ oxidation reaction we studied here, we could quantify the HQ adsorption equilibrium constant (that is, a thermodynamic property of the surface chemisorption reaction) at nanometre spatial resolution, but we cannot determine the reaction rate of the subsequent catalytic conversion to quinone.

Nevertheless, in the case of photocatalytic degradation of organics for water decontamination, the majority of aqueous contaminants are pollutants with low solubilities in water (for example, polycyclic aromatic hydrocarbons, pesticides, pharmaceuticals and endocrine disrupting compounds)^{35,38,39}. At the low-concentration regime, the degradation reaction rate on the catalyst surface scales linearly with the adsorption equilibrium constant of the reactant^{40,41}. The information on the reactant adsorption could thus guide the design of photocatalysts to maximize pollutant degradation reaction kinetics.

COMPEITS is well poised to provide spatially resolved, quantitative information on molecular adsorption on solid surfaces, which is a fundamental phenomenon that has broad implications in various fields of inquiry (Supplementary Section 2.1). For example, COMPEITS could be used to reveal optimal binding sites and thus predict the optimal size, shape, or their combination, for an adsorbent material to achieve high separation efficiency, low energy cost and enhanced molecular selectivity. Such design rules are of paramount importance for chemical separation processes^{35,42–44}, which account for about 10–25% of the world's energy consumption^{45,46}. More broadly, COMPEITS is a potentially powerful tool for advancing materials science and nanotechnology. COMPEITS is suitable for elucidating the molecular binding processes that occur in several material systems of imminent importance, such as graphene-based materials⁴⁷ and covalent organic frameworks⁴⁸. Such knowledge would be directly conducive to addressing fundamental

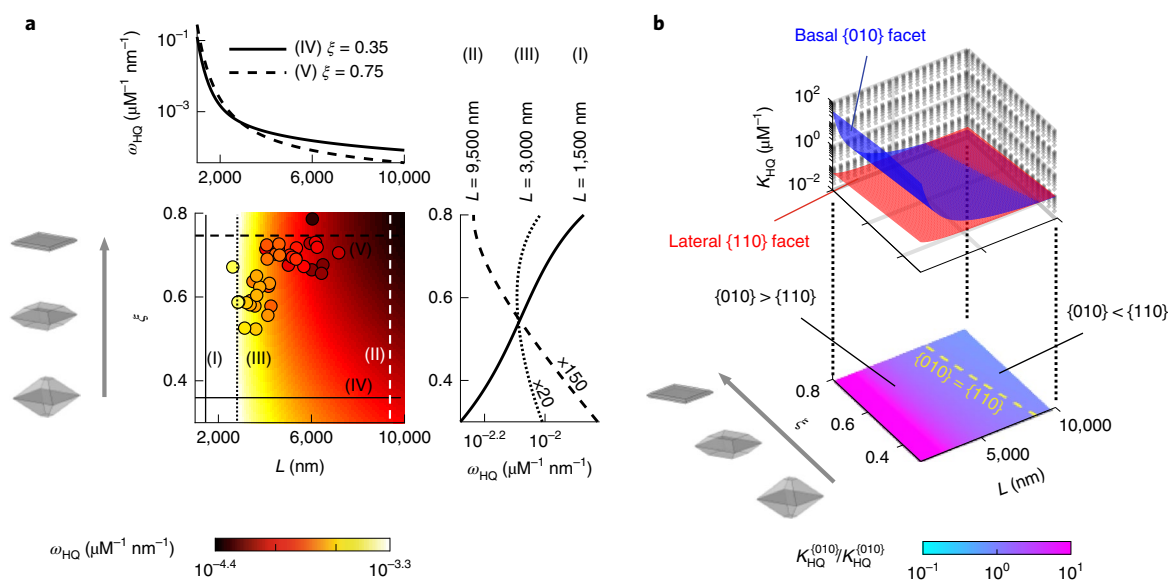


Figure 4 | Rational design of size- and shape-tunable BiVO_4 particles for optimal reactant adsorption. **a**, Bottom-left, the two-dimensional (2D) dependences of ω_{HQ} , which quantifies a particle's overall capability to adsorb HQ on its entire surface at the per-unit-mass level, on L and ξ . Each circle represents one particle of a total of 42 particles. The shaded surface represents predicted values using the fitted parameters β_i of dissected facets from Fig. 3a,b. (I)–(V) denote the line profiles on the shaded surface, which are shown in the top and right panels. Top, the L dependence of ω_{HQ} at selected ξ values (that is, line profiles (IV) and (V)) is shown, demonstrating that plate-like particles display steeper decays with L than bipyramid-like particles. Right, the ξ dependence of ω_{HQ} at selected L values (that is, line profiles (I)–(III)) is shown, demonstrating three distinct ξ dependences at different particle size regimes. **b**, Top, a comparison of $K_{\text{HQ}}^{(010)}$ and $K_{\text{HQ}}^{(110)}$ values over the accessible ranges of L and ξ , showing that the relative magnitude between $K_{\text{HQ}}^{(010)}$ and $K_{\text{HQ}}^{(110)}$ depend on both L and ξ . Bottom, $K_{\text{HQ}}^{(010)}/K_{\text{HQ}}^{(110)}$ versus L and ξ is shown. The yellow dashed line is where $K_{\text{HQ}}^{(010)} = K_{\text{HQ}}^{(110)}$.

questions in materials engineering, such as where small molecules bind preferentially (for example, edge sites versus basal plane in 2D materials), and how the distribution of binding locations affects the optical, electronic and magnetic properties of these materials.

Methods

Synthesis of BiVO_4 particles with a truncated bipyramid morphology. BiVO_4 particles were synthesized by a hydrothermal procedure using a modified method reported by Li et al.³³. Typically, 3 mmol NH_4VO_3 and 3 mmol $\text{Bi}(\text{NO}_3)_3 \cdot 5\text{H}_2\text{O}$ were dissolved in 30 ml of 1 M nitric acid solution, and the resulting solution was adjusted to about pH 1 with ammonia solution. Next, the solution was hydrothermally treated at 80 °C for 48 h, and the yellow solid powder was then separated by filtration, followed by washing with water and drying in air at 60 °C for 24 h.

Ensemble photoelectrochemical measurements. Ensemble-level photoelectrochemical measurements were performed with a potentiostat in a three-electrode configuration using BiVO_4 -modified ITO as the working electrode (prepared by drop-casting 0.5 ml of 10 mg ml⁻¹ BiVO_4 suspensions onto an ITO-coated slide, followed by annealing at 450 °C for 1 h), a Pt wire as the counter electrode and a Ag/AgCl electrode as the reference electrode. A quartz cell with dimensions of 1 cm × 4 cm × 4 cm was employed as the working electrode chamber, which can be illuminated by an expanded 405 nm laser beam with a radius of 1.2 cm and a power density of 5.3×10^{-3} W cm⁻². The working electrode chamber was kept under an N_2 atmosphere, and separated from the counter electrode chamber by a salt bridge. The electrolyte solution was deaerated 0.1 M Na_2SO_4 , 0.1 M pH 7.4 phosphate buffer.

COMPEITS imaging experiments and data analysis. A schematic of the COMPEITS imaging experimental set-up is shown in Supplementary Fig. 2 (similar to Fig. 1a), which is based on single-molecule fluorescence microscopy^{20,21,23,24,49–51} with two-laser epifluorescence illumination on an inverted OLYMPUS IX71 microscope. BiVO_4 particles were spin-coated onto an ITO electrode and annealed at 450 °C for 1 h, and then assembled into a three-electrode photoelectrochemical microfluidic cell (about 5-mm wide and 100- μm high) using double-sided tape sandwiched between an ITO electrode and a coverslip. The reactant solution (deaerated 0.1 M Na_2SO_4 , 0.1 M pH 7.4 phosphate buffer with appropriate quantities of AR and HQ) was continuously supplied to the photoelectrochemical cell at a volumetric flow rate of 25 $\mu\text{l min}^{-1}$. The ITO electrode with dispersed BiVO_4 particles serves as the working electrode, the potential of which was controlled to be at 0.2 V by a potentiostat, and a platinum

wire and a Ag/AgCl electrode were used as the counter and reference electrode, respectively. A continuous-wave circularly polarized 405 nm laser excites the BiVO_4 particles to generate charge carriers, and a 532 nm laser induces the fluorescence of the product resorufin. The two lasers were combined via a 425 nm long-pass dichroic mirror, focused onto the back aperture of a $\times 60$ water immersion objective, and reflected by a 550 nm long-pass dichroic mirror to illuminate the sample in an epi-illumination geometry over a $70 \times 60 \mu\text{m}^2$ area. The fluorescence was collected through the same $\times 60$ objective, passed through the 550 nm long-pass dichroic mirror and a 580 ± 30 nm emission filter, and imaged by an electron-multiplying charge-coupled device camera that was operated at a frame rate of 15-ms, which is controlled by the ANDOR IQ3 software⁵².

First, to obtain the steady photoluminescence intensities of BiVO_4 particles (see Supplementary Section 1.4.1), we collected 1,000 fluorescence images in the absence of the fluorogenic reactant (that is, AR), followed by collecting another 30,000 fluorescence images with appropriate quantities of AR and HQ. In a typical COMPEITS measurement, AR titration experiments (Supplementary Fig. 3) in the absence of HQ ([AR]: 2–100 μM ; 405 nm laser power density: 3.1×10^{-2} W cm⁻²; 532 nm laser power density: 1.8×10^2 W cm⁻²) were performed first to determine K_{AR} . Next, HQ titration experiments in the presence of AR (Supplementary Fig. 15) ([AR]: 50 nM; [HQ]: 0–2 mM; 405 nm laser power density: 1.2×10^2 W cm⁻²; 532 nm laser power density: 1.8×10^2 W cm⁻²) were carried out with the same set of BiVO_4 particles as those in the AR titration experiments to determine K_{HQ} via equation (1) by using the pre-quantified K_{AR} (that is, the HQ titration data were fitted with equation (1) using two floating parameters, k_{AR} and K_{HQ} , and a fixed value for K_{AR}). The fluorescence images were analysed using a home-written MATLAB program, iQPALM (image-based quantitative photoactivated localization microscopy), the details of which have been reported in our previous study⁵³; in this work, a few modifications were made and are detailed in Supplementary Section 1.4. Briefly, the fluorescence images first underwent corrections for the microscope stage drift and the photoluminescence of BiVO_4 , followed by 2D Gaussian fitting to localize the positions of individual fluorescent product molecules, as well as a subsequent filtering process based on a quantitative single-molecule counting algorithm to remove noise contributions and spurious detections, and correct for unresolved multiple-molecule detections.

Representative fluorescence videos of AR oxidation before and after introducing the competing HQ oxidation reaction are shown in the Supplementary Information. There is no discernible difference in the photophysics of the probe molecule before and after introducing HQ (that is, the product molecule resorufin from AR oxidation) (Supplementary Fig. 19). The equations for calculating the specific reaction rate for the whole BiVO_4 crystal, basal {010} facet, lateral {110} facet, type-I edge, and type-II edge are summarized in Supplementary Tables 2 and 3.

Data availability

The data that support the findings of this study are available from the corresponding author on reasonable request.

Code availability

The MATLAB codes that support the findings of this study are available from the corresponding author on reasonable request.

Received: 6 November 2018; Accepted: 31 May 2019;

Published online: 08 July 2019

References

- Jiang, Y. et al. Electron ptychography of 2D materials to deep sub-ångström resolution. *Nature* **559**, 343–349 (2018).
- Fan, C. et al. X-ray and cryo-EM structures of the mitochondrial calcium uniporter. *Nature* **559**, 575–579 (2018).
- de Smit, E. et al. Nanoscale chemical imaging of a working catalyst by scanning transmission X-ray microscopy. *Nature* **456**, 222–225 (2008).
- Wu, C. Y. et al. High-spatial-resolution mapping of catalytic reactions on single particles. *Nature* **541**, 511–515 (2017).
- Jaramillo, T. F. et al. Identification of active edge sites for electrochemical H₂ evolution from MoS₂ nanocrystals. *Science* **317**, 100–102 (2007).
- Tao, F. et al. Break-up of stepped platinum catalyst surfaces by high CO coverage. *Science* **327**, 850–853 (2010).
- von Diezmann, A., Shechtman, Y. & Moerner, W. E. Three-dimensional localization of single molecules for super-resolution imaging and single-particle tracking. *Chem. Rev.* **117**, 7244–7275 (2017).
- Betzig, E. et al. Imaging intracellular fluorescent proteins at nanometer resolution. *Science* **313**, 1642–1645 (2006).
- Gaiduk, A., Yorulmaz, M., Ruijgrok, P. V. & Orrit, M. Room-temperature detection of a single molecule's absorption by photothermal contrast. *Science* **330**, 353–356 (2010).
- Fang, Y. M. et al. Intermittent photocatalytic activity of single CdS nanoparticles. *Proc. Natl Acad. Sci. USA* **114**, 10566–10571 (2017).
- Hell, S. W. & Wichmann, J. Breaking the diffraction resolution limit by stimulated-emission: stimulated-emission-depletion fluorescence microscopy. *Opt. Lett.* **19**, 780–782 (1994).
- Betzig, E. et al. Imaging intracellular fluorescent proteins at nanometer resolution. *Science* **313**, 1642–1645 (2006).
- Rust, M. J., Bates, M. & Zhuang, X. W. Sub-diffraction-limit imaging by stochastic optical reconstruction microscopy (STORM). *Nat. Methods* **3**, 793–795 (2006).
- Sengupta, P., van Engelenburg, S. B. & Lippincott-Schwartz, J. Superresolution imaging of biological systems using photoactivated localization microscopy. *Chem. Rev.* **114**, 3189–3202 (2014).
- Hauser, M. et al. Correlative super-resolution microscopy: new dimensions and new opportunities. *Chem. Rev.* **117**, 7428–7456 (2017).
- Bintu, B. et al. Super-resolution chromatin tracing reveals domains and cooperative interactions in single cells. *Science* **362**, eaau1783 (2018).
- Gustavsson, A. K., Petrov, P. N., Lee, M. Y., Shechtman, Y. & Moerner, W. E. 3D single-molecule super-resolution microscopy with a tilted light sheet. *Nat. Commun.* **9**, 123 (2018).
- Balzarotti, F. et al. Nanometer resolution imaging and tracking of fluorescent molecules with minimal photon fluxes. *Science* **355**, 606–612 (2017).
- Nixon-Abell, J. et al. Increased spatiotemporal resolution reveals highly dynamic dense tubular matrices in the peripheral ER. *Science* **354**, aaf3928 (2016).
- Ristanovic, Z., Kubarev, A. V., Hofkens, J., Roefiaers, M. B. J. & Weckhuysen, B. M. Single molecule nanospectroscopy visualizes proton-transfer processes within a zeolite crystal. *J. Am. Chem. Soc.* **138**, 13586–13596 (2016).
- Tachikawa, T., Yonezawa, T. & Majima, T. Super-resolution mapping of reactive sites on titania-based nanoparticles with water-soluble fluorogenic probes. *ACS Nano* **7**, 263–275 (2013).
- Sambur, J. B. et al. Sub-particle reaction and photocurrent mapping to optimize catalyst-modified photoanodes. *Nature* **530**, 77–80 (2016).
- Zhang, Y. W. et al. Superresolution fluorescence mapping of single-nanoparticle catalysts reveals spatiotemporal variations in surface reactivity. *Proc. Natl Acad. Sci. USA* **112**, 8959–8964 (2015).
- Chen, T. et al. Optical super-resolution imaging of surface reactions. *Chem. Rev.* **117**, 7510–7537 (2017).
- Roefiaers, M. B. et al. Spatially resolved observation of crystal-face-dependent catalysis by single turnover counting. *Nature* **439**, 572–575 (2006).
- Xu, W., Kong, J. S., Yeh, Y. T. & Chen, P. Single-molecule nanocatalysis reveals heterogeneous reaction pathways and catalytic dynamics. *Nat. Mater.* **7**, 992–996 (2008).
- Mo, G. C. H. et al. Genetically encoded biosensors for visualizing live-cell biochemical activity at super-resolution. *Nat. Methods* **14**, 427–434 (2017).
- Folling, J. et al. Fluorescence nanoscopy by ground-state depletion and single-molecule return. *Nat. Methods* **5**, 943–945 (2008).
- Huang, H., Dorn, A., Nair, G. P., Bulovic, V. & Bawendi, M. G. Bias-induced photoluminescence quenching of single colloidal quantum dots embedded in organic semiconductors. *Nano Lett.* **7**, 3781–3786 (2007).
- Oishi, M., Tamura, A., Nakamura, T. & Nagasaki, Y. A smart nanoprobe based on fluorescence-quenching pegylated nanogels containing gold nanoparticles for monitoring the response to cancer therapy. *Adv. Funct. Mater.* **19**, 827–834 (2009).
- Sivula, K. & van de Krol, R. Semiconducting materials for photoelectrochemical energy conversion. *Nat. Rev. Mater.* **1**, 15010 (2016).
- Kim, T. W. & Choi, K. S. Nanoporous BiVO₄ photoanodes with dual-layer oxygen evolution catalysts for solar water splitting. *Science* **343**, 990–994 (2014).
- Li, R. G. et al. Spatial separation of photogenerated electrons and holes among {010} and {110} crystal facets of BiVO₄. *Nat. Commun.* **4**, 1432 (2013).
- Brandl, F., Bertrand, N., Lima, E. M. & Langer, R. Nanoparticles with photoinduced precipitation for the extraction of pollutants from water and soil. *Nat. Commun.* **6**, 7765 (2015).
- Alsbaiee, A. et al. Rapid removal of organic micropollutants from water by a porous β -cyclodextrin polymer. *Nature* **529**, 190–194 (2016).
- Thomas, A. G. & Syres, K. L. Adsorption of organic molecules on rutile TiO₂ and anatase TiO₂ single crystal surfaces. *Chem. Soc. Rev.* **41**, 4207–4217 (2012).
- Voet, D., Voet, J. G. & Pratt, C. W. *Fundamentals of Biochemistry: Life at the Molecular Level* 4th edn (Wiley, 2013).
- Schwarzenbach, R. P. et al. The challenge of micropollutants in aquatic systems. *Science* **313**, 1072–1077 (2006).
- Shannon, M. A. et al. Science and technology for water purification in the coming decades. *Nature* **452**, 301–310 (2008).
- Zhou, X. C., Xu, W. L., Liu, G. K., Panda, D. & Chen, P. Size-dependent catalytic activity and dynamics of gold nanoparticles at the single-molecule level. *J. Am. Chem. Soc.* **132**, 138–146 (2010).
- Zhou, X. C. et al. Quantitative super-resolution imaging uncovers reactivity patterns on single nanocatalysts. *Nat. Nanotechnol.* **7**, 237–241 (2012).
- Cadiou, A. et al. Hydrolytically stable fluorinated metal-organic frameworks for energy-efficient dehydration. *Science* **356**, 731–735 (2017).
- Sung Cho, H. et al. Extra adsorption and adsorbate superlattice formation in metal-organic frameworks. *Nature* **527**, 503–507 (2015).
- Alvarez, P. J. J., Chan, C. K., Elimelech, M., Halas, N. J. & Villagran, D. Emerging opportunities for nanotechnology to enhance water security. *Nat. Nanotechnol.* **13**, 634–641 (2018).
- Sholl, D. S. & Lively, R. P. Seven chemical separations to change the world. *Nature* **532**, 435–437 (2016).
- Mao, X. et al. Energetically efficient electrochemically tunable affinity separation using multicomponent polymeric nanostructures for water treatment. *Energy Environ. Sci.* **11**, 2954–2963 (2018).
- Shi, G. et al. Two-dimensional NaCl crystals of unconventional stoichiometries on graphene surface from dilute solution at ambient conditions. *Nat. Chem.* **10**, 776–779 (2018).
- Li, J. et al. ⁹⁹TcO₄⁻ remediation by a cationic polymeric network. *Nat. Commun.* **9**, 3007 (2018).
- Hodgson, G. K., Impellizzeri, S. & Scaiano, J. C. Dye synthesis in the pechmann reaction: catalytic behaviour of samarium oxide nanoparticles studied using single molecule fluorescence microscopy. *Chem. Sci.* **7**, 1314–1321 (2016).
- Chen, P. et al. Spatiotemporal catalytic dynamics within single nanocatalysts revealed by single-molecule microscopy. *Chem. Soc. Rev.* **43**, 1107–1117 (2014).
- Ng, J. D. et al. Single-molecule investigation of initiation dynamics of an organometallic catalyst. *J. Am. Chem. Soc.* **138**, 3876–3883 (2016).
- ANDOR IQ v3 (Oxford Instruments, 2019).
- Chen, T. Y. et al. Concentration- and chromosome-organization-dependent regulator unbinding from DNA for transcription regulation in living cells. *Nat. Commun.* **6**, 7445 (2015).

Acknowledgements

The research on water pollutant degradation and super-resolution mapping was funded by the Army Research Office (grant no. W911NF-17-1-0590, and in part grant no. W911NF-18-1-0217). The research on BiVO₄ synthesis, characterization and photoelectrochemistry was funded by the US Department of Energy, Office of Science, Basic Energy Sciences, Catalysis Science Program (grant no. DE-SC0004911). This research made use of the Cornell Center for Materials Research Shared Facilities, which are supported through the NSF MRSEC program (grant no. DMR-1719875). We thank W. Jung and G. Chen for helpful discussions on instrument construction and data analysis.

Author contributions

X.M., C.L. and P.C. designed the research. X.M. synthesized the catalysts, constructed the instruments, performed the measurements, coded the software and analysed the data. X.M. and P.C. discussed the results and wrote the manuscript. M.H. and N.Z. contributed to the experiments.

Competing interests

X.M. and P.C. have filed a provisional patent application 'A competition-enabled imaging technique with super-resolution' on 27 September 2018 with the US Patent Office (Provision Number 62/737,195).

Additional information

Supplementary information is available for this paper at <https://doi.org/10.1038/s41557-019-0288-8>.

Reprints and permissions information is available at www.nature.com/reprints.

Correspondence and requests for materials should be addressed to P.C.

Publisher's note: Springer Nature remains neutral with regard to jurisdictional claims in published maps and institutional affiliations.

© The Author(s), under exclusive licence to Springer Nature Limited 2019